

PAPER • OPEN ACCESS

Time-invariant component-based normalization for a simultaneous PET-MR scanner

To cite this article: M A Belzunce and A J Reader 2016 *Phys. Med. Biol.* **61** 3554

View the [article online](#) for updates and enhancements.

You may also like

- [Utilization of Digital Image Processing In Process of Quality Control of The Primary Packaging of Drug Using Color Normalization Method](#)
Danang Erwanto, Sri Artini Dwi Prasetyowati and Eka Nuryanto Budi Susila
- [Normalization and weighting methods for precise and standardized sustainability assessment: recent practices in manufacturing](#)
S Ahmad, K Y Wong, I Zahid et al.
- [Influence of Normalization Techniques on Multi-criteria Decision-making Methods](#)
Sandile Thamie Mhlanga and Manoj Lall

Time-invariant component-based normalization for a simultaneous PET-MR scanner

M A Belzunce and A J Reader

King's College London, Division of Imaging Sciences & Biomedical Engineering, 3rd Floor Lambeth Wing, St Thomas' Hospital, London, SE1 7EH, UK

E-mail: martin.belzunce@kcl.ac.uk

Received 23 October 2015, revised 8 March 2016

Accepted for publication 16 March 2016

Published 7 April 2016



CrossMark

Abstract


Component-based normalization is a method used to compensate for the sensitivity of each of the lines of response acquired in positron emission tomography. This method consists of modelling the sensitivity of each line of response as a product of multiple factors, which can be classified as time-invariant, time-variant and acquisition-dependent components. Typical time-variant factors are the intrinsic crystal efficiencies, which are needed to be updated by a regular normalization scan. Failure to do so would in principle generate artifacts in the reconstructed images due to the use of out of date time-variant factors. For this reason, an assessment of the variability and the impact of the crystal efficiencies in the reconstructed images is important to determine the frequency needed for the normalization scans, as well as to estimate the error obtained when an inappropriate normalization is used. Furthermore, if the fluctuations of these components are low enough, they could be neglected and nearly artifact-free reconstructions become achievable without performing a regular normalization scan. In this work, we analyse the impact of the time-variant factors in the component-based normalization used in the Biograph mMR scanner, but the work is applicable to other PET scanners. These factors are the intrinsic crystal efficiencies and the axial factors. For the latter, we propose a new method to obtain fixed axial factors that was validated with simulated data. Regarding the crystal efficiencies, we assessed their fluctuations during a period of 230 d and we found that they had good stability and low dispersion. We studied the impact of not including the intrinsic crystal efficiencies in the normalization when reconstructing



Original content from this work may be used under the terms of the [Creative Commons Attribution 3.0 licence](https://creativecommons.org/licenses/by/3.0/). Any further distribution of this work must maintain attribution to the author(s) and the title of the work, journal citation and DOI.

simulated and real data. Based on this assessment and using the fixed axial factors, we propose the use of a time-invariant normalization that is able to achieve comparable results to the standard, daily updated, normalization factors used in this scanner. Moreover, to extend the analysis to other scanners, we generated distributions of crystal efficiencies with greater fluctuations than those found in the Biograph mMR scanner and evaluated their impact in simulations with a wide variety of noise levels. An important finding of this work is that a regular normalization scan is not needed in scanners with photodetectors with relatively low dispersion in their efficiencies.

Keywords: crystal efficiencies, image reconstruction, component-based normalization, time-invariant normalization, normalization

 Online supplementary data available from stacks.iop.org/PMB/61/3554/mmedia

(Some figures may appear in colour only in the online journal)

1. Introduction

Component-based normalization (CBN) is widely used to compensate for the differences in the sensitivity of each of the lines of response (LORs) acquired in positron emission tomography (PET). This method consists of modelling the sensitivity of each LOR as a product of multiple factors (Casey *et al* 1995, Badawi and Marsden 1999, Bai *et al* 2002). As a consequence, the parameters to be estimated are considerably fewer than the number of LORs and, therefore, they can be computed from relatively short duration normalization scans.

In the CBN, the components can be separated into time-invariant (e.g. geometry and block profile), time-variant (e.g. intrinsic crystal efficiencies) and acquisition-dependent (dead-time) components. Typical time-variant factors are the intrinsic crystal efficiencies, that depend on the technology of the scanner's detectors and the environmental conditions (e.g. temperature). The term intrinsic crystal efficiency, or simply, crystal efficiency will be used in this work since its the term used by the manufacturers and in the literature, but in fact its the effective efficiency of the crystal with the photodetector and electronics associated with it. These factors are needed to be updated by regular scans to avoid normalization artifacts. The frequency of these scans depends on the variability and dispersion of the crystal efficiencies. An assessment of the variations of the crystal efficiencies is important to find out the consequences of not using the correct crystal efficiencies, whether because the normalization scan was not available or out of date, or because the operating conditions changed since the last scan. Even more, if the fluctuations are low enough, the impact of the time-variant components can be potentially neglected and artifact-free reconstructions can be achieved without performing a regular normalization scan.

In this work, we analyse the CBN used in the Biograph mMR PET-MR scanner (Siemens Healthcare, Erlangen, Germany), which uses avalanche photodiodes (APDs) (Delso *et al* 2011). We focused on the impact of the crystal efficiencies as they are the main time-variant normalization factors, and because the efficiency of APD's is very sensitive to the operating temperature and the bias voltage (Roncali and Cherry 2011). For that reason the room temperature needs to be kept as stable as possible and frequent normalization scans are recommended (Keereman *et al* 2012). We assessed the fluctuations of these factors over a period of 230 d. In addition, we study the impact of the time-variant axial factors. For the latter, we propose a

new model to replace them with fixed factors, which is applicable to other PET scanners. We show, by reconstructing real phantom data, that the time-variant component has a low impact for the Biograph mMR scanner under normal working conditions. Moreover, we simulated distributions of crystal efficiencies with greater fluctuations than those found in the Biograph mMR scanner and evaluated their impact on reconstructed images from simulated sinograms with a wide variety of noise levels. Finally, we show that using the newly proposed time-invariant normalization, we can achieve equivalent results to the standard normalization used in the Biograph mMR scanner. The method can be applied to scanners with photodetectors with low gain dispersion, or with a temperature-dependent gain control module, eliminating the need to have a daily or weekly normalization scan. For scanners with a higher standard deviation in their photodetectors, the time-invariant normalization could be used as an initial estimate in a self-normalization algorithm.

2. Theory

The normalization factors (N) model the efficiency of each sinogram bin and are stored in a diagonal matrix with as many rows and columns as the total number of bins in the sinogram. In the forward model for the expectation maximization (EM) reconstruction, N is a multiplicative factor (see e.g. Reader and Zaidi (2007)):

$$q = A \cdot N \cdot X \cdot f + s + r \quad (1)$$

where A are the attenuation factors, N the normalization factors, X is the x-ray transform that projects image f into a sinogram, and s and r are the scatter and randoms estimates respectively. In equation (1) capitals denote matrices, and lower case letters denote vectors.

2.1. A model for component-based normalization

Complete models for the CBN have been presented by different authors (Casey *et al* 1995, Badawi *et al* 1998, Bai *et al* 2002). In the case of the mMR scanner, the normalization model used is:

$$N(i) = \varphi_r \cdot \epsilon_{d1} \cdot \epsilon_{d2} \cdot ci_{r,\theta} \cdot ap_z \cdot d_{d1} \cdot d_{d2} \quad (2)$$

where

- $N(i)$ is the normalization factor for sinogram bin i , stored at row and column index i of the diagonal matrix N . The bin i has coordinates (i_θ, i_r, i_z) , with i_θ and i_r being the indices of the azimuthal angle θ and the radial distance r ; and i_z is the sinogram plane index, which is a linear index that depends on the rings r_1 and r_2 of the LOR represented in bin i .
- φ_r is a geometric factor that depends on the angle of incidence of the photon onto the detector. It depends only on the radial position (r) of the LOR represented in bin i .
- ϵ_{d1} and ϵ_{d2} are the intrinsic efficiencies of the two crystals $d1$ and $d2$ that form the LOR represented in bin i .
- $ci_{r,\theta}$ is a factor that accounts for the crystal interference pattern generated by the block profile of efficiencies in the transverse plane. This profile is a systematic variation in the crystal efficiencies that depends on the transaxial positions of each crystal's pixel within the detector block and the angle of the projection.
- ap_z is an axial factor that includes the variations in the plane efficiencies due to geometric properties and to the crystal interference pattern that is also formed in the axial direction. In addition, it accounts for the number of sinograms compressed into the plane i_z (span factor).

- d_{d1} and d_{d2} are the dead-time factors for the two detectors involved in detecting the LOR represented in bin i .

If more than one LOR is represented in a sinogram bin, the average normalization factors of the group of LORs is used.

2.2. Component classification

The CBN components can be classified as time-invariant, time-variant and acquisition-dependent:

$$N_C = N_{TI} \cdot N_{TV} \cdot N_{AQ} \quad (3)$$

where N_C are the complete normalization factors (also named N in equation (2)), N_{TI} are the time-invariant, N_{TV} are the time-variant and N_{AQ} the acquisition-dependent components. The N_{TI} components are those that do not change with time, for example those related to the geometric properties of the scanner. The N_{TV} factors are dependent upon the intrinsic crystal efficiencies and other factors related to them (e.g. axial factors), since they usually present temporal variations due to changes in the room temperature or drifts in the gains of the PMTs or APDs. Finally the N_{AQ} is composed of the dead-time component that depends on the count rate in each detector during a given scan.

3. Component-based normalization of the Biograph mMR scanner

3.1. The Biograph mMR scanner

In this work, we focus on the CBN used by the Biograph mMR scanner, which is composed of 8 rings of 56 detector blocks each. Each block is composed of 8×8 crystal elements of LSO, making up a total of 64 rings of 448 crystal elements. The standard image reconstruction for this scanner uses 3D span-11 sinograms, with 837 sinogram planes of 344 (radial coordinate) \times 252 (angle projection) bins. The gaps between each block are also represented in the sinograms by using an additional crystal element with zero-gain. Therefore, the sinograms are generated by virtual blocks of 9 (transverse) \times 8 (axial) crystal elements. In its daily use in St. Thomas' Hospital, the scanner is powered on and off every day, as was advised by the manufacturer, since the scanner is not used overnight. For this reason, it was suggested by the manufacturer to perform a daily ^{68}Ge normalization scan.

3.2. The Biograph mMR normalization file

The Biograph mMR scanner uses a normalization file with 7 fields to account for the model described in section 2.1. The components, available for span-11 sinograms only, are: geometric effects, crystal interference, crystal efficiencies, axial effects, paralyzing ring dead-time parameters, non-paralyzing ring dead-time parameters and additional axial effects. In the supplementary material a detailed description of each component is found (stacks.iop.org/PMB/61/3554/mmedia).

In the CBN of the Biograph mMR scanner, the time-variant factors are the crystal efficiencies and the axial factors, both being studied in this work. The axial factors depend on the geometry and on the crystal efficiencies. As well as for the transverse plane, the crystal efficiencies can be split into a fixed profile factor and a variable determined by the intrinsic crystal efficiencies. In this paper, we propose a new model to obtain fixed axial factors for both span-1 and span-11 sinograms.

3.3. Crystal efficiencies

We studied the crystal efficiencies over a time span of 230 d by using 92 normalization scans performed in that period. The coefficient of variation (COV) for all the data sets was only 2.86%. The median, minimum and maximum values were also computed. These metrics are shown in figure 1, where it can be seen that the standard deviation of the crystal efficiencies is stable over time with the exception of a few measurements (visible with a larger error bar).

To generate the normalization factors, the crystal efficiencies need to be converted into a normalization sinogram, where each bin is the multiplication of the two crystal efficiencies involved in a given sinogram bin (see the supplementary material for more details).

3.4. Axial factors

The axial factors take into account the number of LORs axially compressed, the axial crystal interference pattern and the detection efficiency. For the Biograph mMR scanner, these factors are stored in two components: the so-called ‘axial effects’ factors and the ‘additional axial effects’ factors. Each of them is an array with 837 elements, one for each plane of the span-11 sinograms. Just as for the crystal efficiencies, we studied their variability in the 92 normalization data sets by computing the mean value and standard deviation of both axial components (figure 2).

The COV was lower than 1% for every sinogram plane, being almost invariable with time. For that reason, we propose a method to estimate time-invariant axial factors to be used as a fixed component of the N_{TI} . This method allows the estimation of axial factors for sinograms without axial compression (span-1) or with any axial compression different to 11. To achieve this, we scanned for 5 h a ^{68}Ge uniform cylinder phantom with a total activity of 70 MBq and obtained sinograms without axial compression. In the direct sinograms, a uniform count rate would be expected along the scanner’s field of view; however, the attenuation, the scatter and the randoms generate a non-uniform axial profile. Hence, the counts in each ring depends on a combination of these effects and the detection sensitivity of each of ring. Because we need to estimate the latter, the detection profile must be corrected from the non-uniform incident activity. The axial detected profile, computed as the sum of the counts of each direct sinogram, shows this effect in figure 3(a), where the axial crystal interference pattern is repeated in the 8 blocks, each of them with 8 rings.

The activity profile was computed splitting the rings into groups of crystals with the same position within each block. Each group was normalized to its mean value and then a profile using the normalized counts of all the groups was produced:

$$C_{Nij} = \frac{C_{ij}}{\frac{1}{N_{\text{blocks}}} \cdot \sum_{k=0}^{N_{\text{blocks}}-1} C_{ik}} \quad (4)$$

where C_{ij} are the counts in the crystal ring i of block ring j , N_{blocks} is the number of block rings and C_{Nij} are the normalized counts in the crystal ring i of block ring j .

Using the C_{Nij} parameters, we fitted a 4th order curve (figure 3(b)) that will be used as a reference for the incident activity profile to correct the original counts per sinogram:

$$C_{NCij} = \frac{C_{Nij}}{A_{i+j} \cdot N_{\text{acrystals}}} \quad (5)$$

where C_{NCij} are the corrected and normalized counts in the crystal ring i of block ring j , $N_{\text{acrystals}}$ is the number of crystals in a block in the axial direction and A_r is the incident activity profile for each ring r .

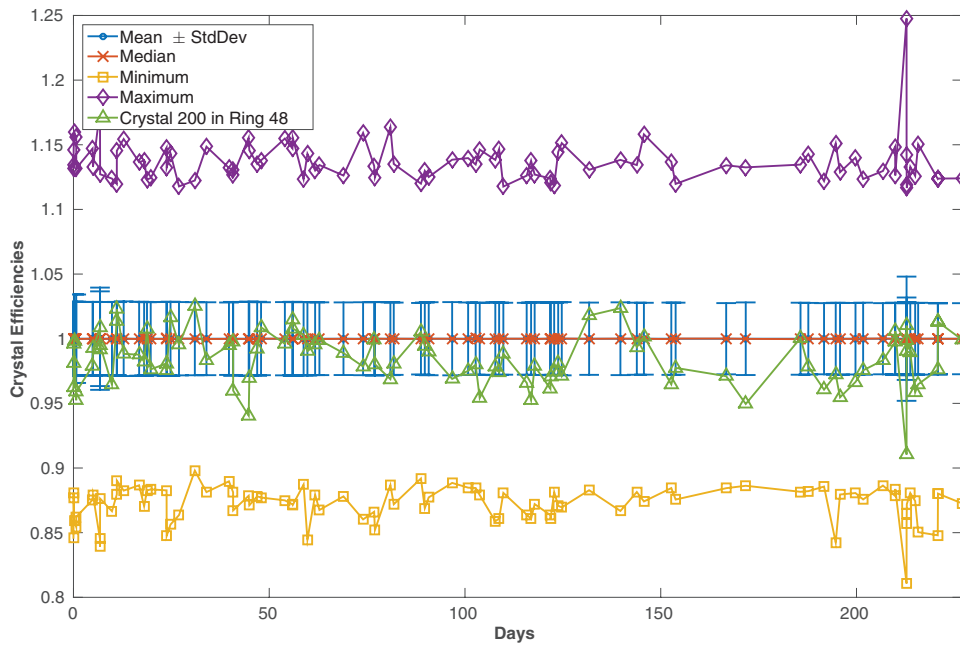


Figure 1. Statistics of the crystal efficiencies based on 92 normalization scans acquired over a period of 230 d. The mean value with the standard deviation (error bars), the median (crosses), the minimum (squares) and maximum (diamonds) values were computed for each crystal efficiencies data set. An example of the efficiency variation of a given crystal is also shown (triangles).

Using the corrected counts per sinogram, we computed the mean block profile for the direct sinograms (figure 3(c)) and then its square root to obtain the detection efficiency profile for a single photon:

$$\epsilon_{axial}(i) = \sqrt{\frac{1}{N_{blocks}} \cdot \sum_{k=0}^{N_{blocks}-1} C_{NCik}} \tag{6}$$

where $\epsilon_{axial}(i)$ is the estimated efficiency for the crystal ring i within a block ring and C_{NCik} are the normalized and corrected counts in the crystal ring i of the block ring k .

Finally, the ring gain for each block ring is used to get an axial factor for each sinogram:

$$N_{AX}(i_z) = \sum_{s=1}^{N_{span}} \epsilon_{axial}(i1) \cdot \epsilon_{axial}(i2) \tag{7}$$

$$i1 = r_1(i_z, s) \text{ mod } N_{paxial} \tag{8}$$

$$i2 = r_2(i_z, s) \text{ mod } N_{paxial} \tag{9}$$

where $N_{AX}(i_z)$ is the axial factor for the sinogram plane i_z , s is one of the N_{span} LORs axially compressed in that plane, and $r_1(s)$ and $r_2(s)$ are the two rings involved in that LOR.

In figure 3(d), the normalization correction factors for the axial block profile are shown for the three first segments of a span-1 sinogram, as well as its application to the sinogram of the ^{68}Ge phantom scan.

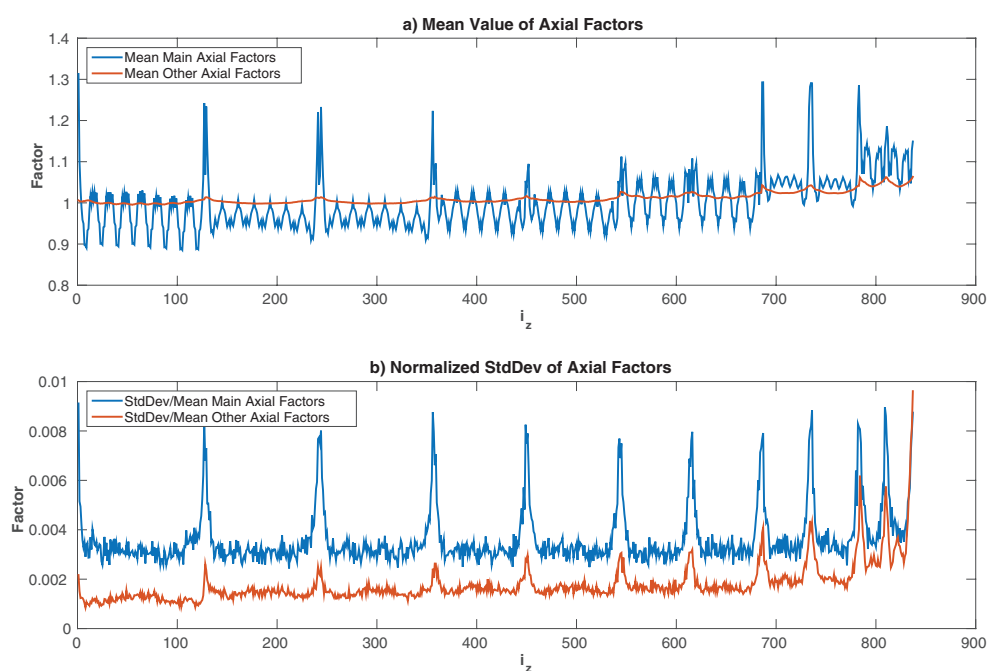


Figure 2. (a) Mean value of the main and other axial factors for the 92 normalization scans. (b) Standard deviation of the main and other axial factors for the 92 normalization scans, normalized to their mean value.

Besides the axial block profile, an additional axial factor is needed to account for the sensitivity of each LOR that depends on the incident angle of the photons. Each segment of the sinogram represents the same azimuthal angle, therefore we computed this additional factor using the mean value of each segment of the span-1 sinogram of the ^{68}Ge phantom scan. Both the axial profile and axial sensitivity factors can be transformed into span-N factors by summing the factors of each plane compressed in a segment.

4. Methods

The impact of the time-variant normalization factors on the reconstructed images was evaluated using real and simulated data. The simulations were used to assess the axial factors and the crystal efficiencies independently, as well as to analyse the impact of sets of crystal efficiencies with a larger standard deviation than the ones found in the Biograph mMR. In order to evaluate the influence of each factor, we reconstructed the data sets using the complete normalization factors and also with just the time-invariant factors.

The images were reconstructed with a code developed in our laboratory, where an ordinary Poisson ordered subsets expectation maximization (OP-OSEM) was implemented using a Siddon projector/backprojector (Belzunce *et al* 2012). We used span-11 and span-1 reconstructions. Randoms and scatter estimates were included in the forward model for the real data. The scatter was estimated using the single scatter simulation (SSS) algorithm implemented in STIR (Polycarpou *et al* 2011, Thielemans *et al* 2012).

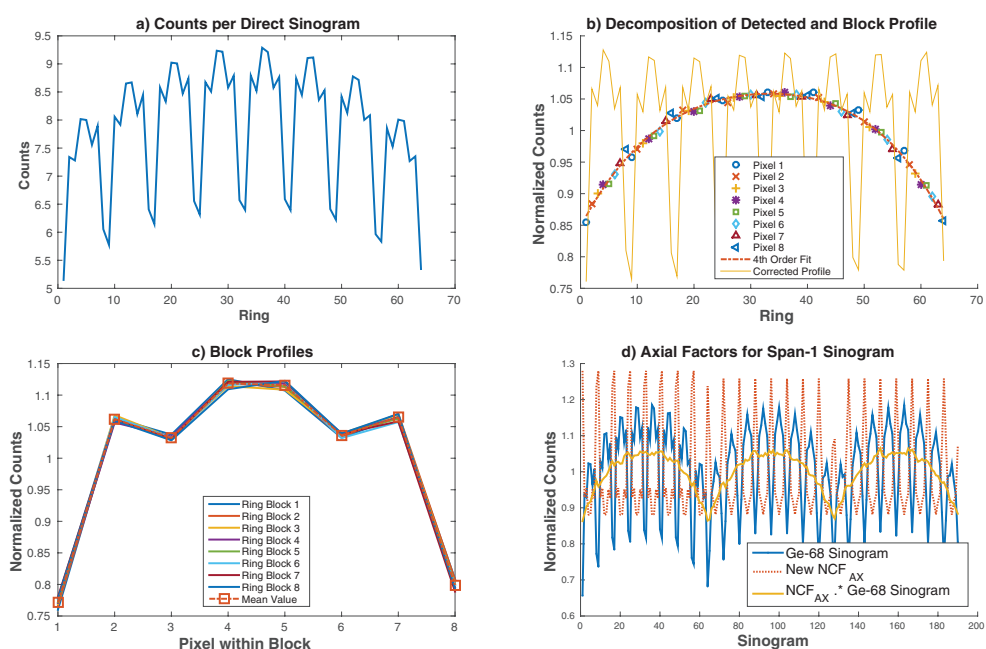


Figure 3. (a) Counts in the direct sinograms of a 5 h ^{68}Ge phantom scan. (b) Counts for each pixel normalized to the mean value of the counts in that pixel position for every block. A fitted 4th order curve for the pixel's normalized counts is shown as a dashed line. The new block profiles after correcting them with the aforementioned curve is also visible. (c) Normalized counts of each block for the profile corrected direct sinograms and their mean value. (d) New axial factors and their application to the ^{68}Ge scan for the first three segments of the span-1 sinogram.

4.1. Normalization factors

In the reconstruction process, we used five different normalization factors:

- Complete normalization factors for span-1 (N_{C-1}) and span-11 (N_{C-11}) sinograms. It includes all the factors of the CBN. For the span-1 reconstruction, we used the fixed axial factors described previously in this paper; while for span-11, we employed the axial factors available in the normalization file.
- Time-invariant normalization factors for span 1 (N_{TI-1}) and span 11 (N_{TI-11}) sinograms. The crystal efficiencies and axial factors were not included, except for the span compression factors (number of LORs axially compressed in each plane).
- Time-invariant normalization factors but including the correct time-variant axial factors, which are only available for span 11 ($N_{TI+AX-11}$).
- Time-invariant normalization factors with modelled axial factors for span-1 ($N_{TI\text{mod}-1}$) and span-11 ($N_{TI\text{mod}-11}$) sinograms, which were computed using the model described in section 3.4. These are the normalization factors that we propose to use for a time-invariant normalization.
- Complete normalization factors for span-11 ($N_{C\text{random}-11}$) from a random normalization file. It is used to test the impact on the reconstruction of using a wrong set of crystal efficiencies.

The crystal efficiencies used to generate the normalization factors for span-11 sinograms were obtained by averaging the products of the crystal efficiencies associated with every detector pair contributing to a given sinogram bin. This method to normalize axially compressed data is equivalent to post-normalization of list-mode data, which has been shown to outperform a pre-normalization strategy (Thielemans *et al* 2008).

4.2. Simulated data

We simulated 4 sets of crystal efficiencies, 3 of them had a normal distribution with 1, 5 and 10 times the standard deviation of the broadest distribution found in the Biograph mMR normalization files (set 1, 2 and 3 respectively). The remaining set had a uniform distribution between 0 and 2 (set 4).

For each set of crystal efficiencies, we simulated 3D sinograms by projecting a phantom and multiplying it by the complete normalization factors (N_{C-1}), thereby introducing a need for normalization in each case. We simulated both span-1 and span-11 sinograms. For the latter, we performed the simulation by projecting the phantom into span-1 sinograms, then applying the N_{C-1} factors and finally compressing them to span-11. On the grounds that the simulation is based on span-1 sinograms and we want to evaluate only the impact of the intrinsic crystal efficiencies, in these simulations we used the modelled fixed axial factors described in section 3.4.

We used a uniform cylinder and a brain phantom (Cocosco *et al* 1997). First, we projected the phantom images to get noise-free sinograms. Then, we introduced noise to them by simulating a Poisson process. A number of different noise levels was simulated by using a global factor that first scaled each noise-free sinogram to get mean bin values of 1 to 200 counts.

To analyse the axial factors, we used a different group of simulations using unit crystal efficiencies, as we are interested in evaluating only the axial factors. In these simulations, we utilized only span-11 sinograms because the Biograph mMR axial factors are only available for that sinogram format. Therefore the N_{C-11} factors were applied directly to the span-11 projected sinograms.

4.3. Real data

To evaluate the impact of using only the time-invariant normalization factors with experimental data, we scanned two phantoms with the Biograph mMR scanner:

- A NEMA image quality phantom filled with a background concentration of 1.5 kBqml^{-1} of ^{18}F and using only cold spheres. The acquired sinogram had around 5.0×10^7 counts. This represents the case of a set of sinograms with a similar level of statistics to a typical clinical acquisition.
- A striatal phantom (model RS-901T, Radiology Support Devices Inc.) filled with ^{18}F with a background activity concentration of 15 kBqml^{-1} and 5 times that activity in the caudate and the putamen. The acquired sinogram had approximately 7.50×10^8 counts, corresponding to a high-statistics set of sinograms.

4.4. Evaluation of the axial factors

Using the simulated data, we reconstructed the span-11 sinograms of the brain phantom using the N_{C-11} , N_{TI-11} and $N_{TI_{\text{mod}}-11}$ normalization factors. In 3D reconstruction, the axial factors

affect mainly, but not only, the axial profile of the reconstructed images. Therefore, for each reconstructed volume we computed the mean value of each slice for the full image and for regions of interest (ROIs) determined by three of the tissues available in the simulated brain phantom: the cerebrospinal fluid (CSF), the gray matter and white matter. Using the simulated phantom as the reference, we computed:

$$\text{RMSE}_{f_{\text{NX}}} = \sqrt{\sum_{i=1}^{N_z} \left(\sum_{j=1}^{N_{\text{ROI}_i}} \frac{f_{\text{phantom}_{ji}}}{N_{\text{ROI}_i}} - \sum_{j=1}^{N_{\text{ROI}_i}} \frac{f_{\text{NX}_{ji}}}{N_{\text{ROI}_i}} \right)^2} \quad (10)$$

where the $\text{RMSE}_{f_{\text{NX}}}$ is the root mean square error (RMSE) of the mean axial values of the image f_{NX} respect to the reference f_{phantom} . j is the index of one of the N_{ROI_i} pixels that belongs to the ROI in slice i . The RMSE values were estimated for the reconstructed images from the noise-free and the noisy simulated sinograms.

4.5. Evaluation of the impact of the crystal efficiencies

The simulations of the uniform cylinder and the brain phantom were used to assess the impact of the crystal efficiencies. The images were reconstructed with the $N_{\text{TI}_{\text{mod}}}$ and N_{C} normalization factors for both span-1 and span-11 sinograms. As was described in section 4.1, the only difference between them is that the latter takes into account the effect of the intrinsic crystal efficiencies.

To evaluate the uniformity of the reconstructed images of the uniform cylinder phantom, we computed the standard deviation, the mean value and then the coefficient of variation (COV) of 9 ROIs of 30 mm diameter in each slice (figure 4(a)). Finally, we computed the mean value of the ROIs COV for each reconstructed image. The simulated brain phantom was also used to assess the crystal efficiencies. In this case, we measured the COV in the putamen, the caudate and the white matter. These regions have low variance in the brain phantom, and they can be seen in figures 4(b)–(d).

Furthermore, we evaluated the standard deviation in uniform regions of the experimental data. For the striatal phantom, we computed the mean value and standard deviation in 4 ROIs of 20 mm diameter in each of the 20 central slices (figure 5(a)). In addition, we estimated the COV of the mean ROI values for each slice:

$$\text{COV}_i = \frac{1}{\mu_{\text{R}_i}} \sqrt{\sum_{k=1}^{N_{\text{R}}} \frac{(\mu_{ki} - \mu_{\text{R}_i})^2}{N_{\text{R}} - 1}} \quad (11)$$

where N_{R} is the number of ROIs used per slice, μ_{ki} is the mean pixel value of the ROI k of slice i and μ_{R_i} is the mean value of all the ROIs within that slice. A similar assessment was carried out for the scanned NEMA image quality phantom. In that case, we used 11 ROIs of 20 mm diameter (figure 5(b)).

5. Results

The axial profiles for the reconstructed images from the noise-free simulations of the brain phantom were computed and they are shown in figure 6, where the mean values per slice were calculated for the full image (figure 6(a)), for the image masked with the CSF ROI (figure 6(b)), with the Gray Matter ROI (figure 6(c)) and with the White Matter ROI (figure 6(d)). In those profiles, there is no visible difference between using the $N_{\text{C}-11}$ and the $N_{\text{TI}_{\text{mod}}-11}$

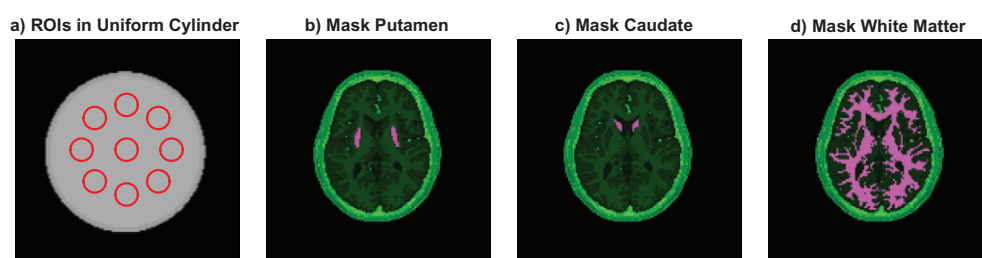


Figure 4. Simulated phantoms and the ROIs used to evaluate the impact of the crystal efficiencies. a) The uniform cylinder phantom and the 9 ROIs used. (b)–(d) The brain phantom and the mask used for the putamen (b), the caudate (c) and the white matter (d).

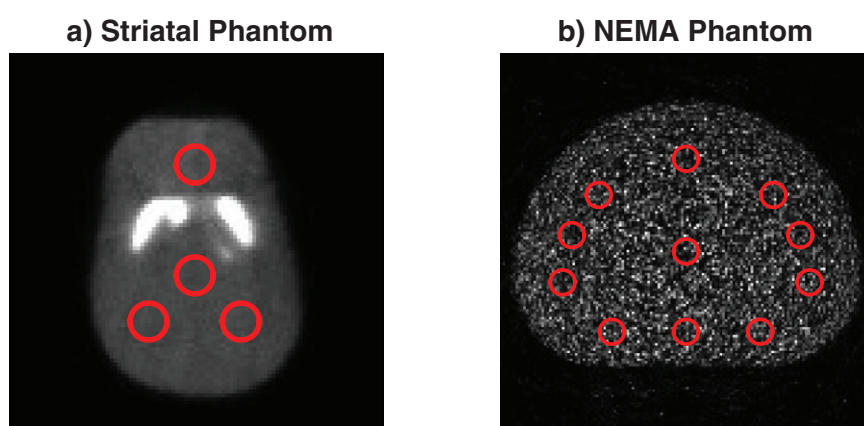


Figure 5. Phantoms scanned with the Biograph mMR. (a) Striatal phantom and the 4 ROIs used to evaluate the noise in the background. (b) NEMA image quality phantom and the 11 ROIs used to evaluate the noise in the background.

normalization factors, showing that the proposed method can match the standard method. On the contrary, the use of only the span axial factor ($N_{\text{TI}-11}$) results in a notably noisier mean value per slice, producing artifacts in the axial direction. This was also observed in the maximum intensity projections of the reconstructed images, where the artifacts are visible in the coronal and sagittal planes (figure 7).

To quantify this outcome, the RMSE values were computed as described in section 4.4. In figure 8, the RMSE of the axial mean values for the noisy simulated sinograms are plotted on a bar graph. Similar results as the ones achieved for the noise free results were obtained, where the reconstructed images reconstructed with the modelled axial factors ($N_{\text{TI}_{\text{mod}}-11}$) had a similar RMSE to the reconstructed with the true axial factors ($N_{\text{C}-11}$). In addition, the use of only the span compression factor ($N_{\text{TI}-11}$) increased the noise in the images even for the noisier simulations.

Regarding the assessment of the crystal efficiencies, we reconstructed both simulated and real data. For the uniform cylinder simulated data, we compared the reconstructed images with the complete normalization factors ($N_{\text{C}-1}$ and $N_{\text{C}-11}$) to those reconstructed without using the crystal efficiencies ($N_{\text{TI}_{\text{mod}}-1}$ and $N_{\text{TI}_{\text{mod}}-11}$). In figures 9(a)–(d), the mean COV of the

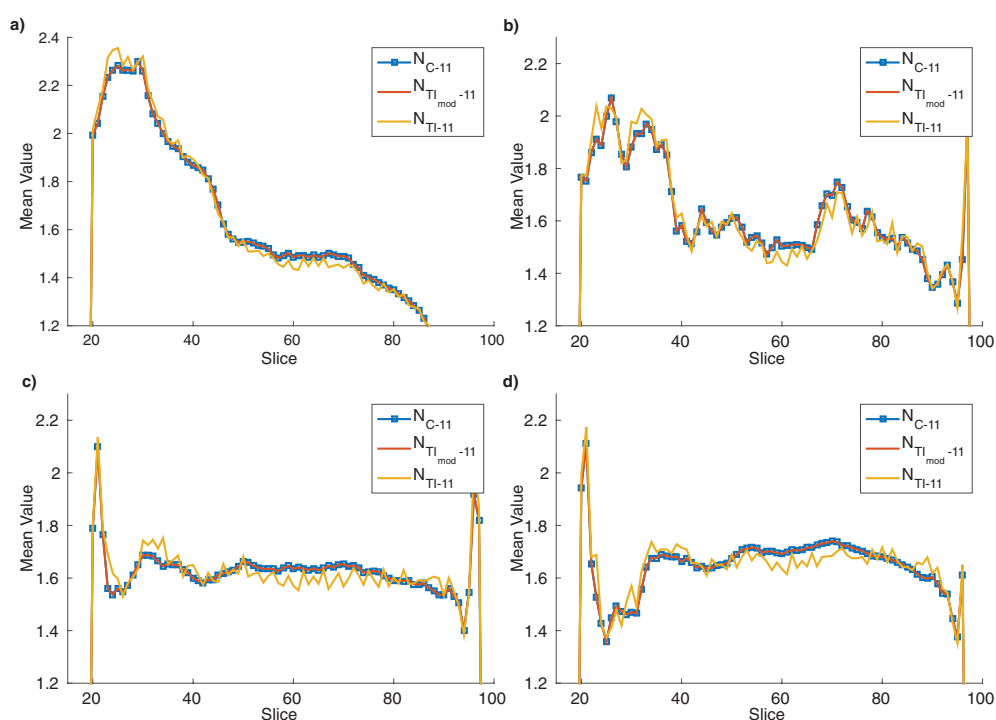


Figure 6. Mean values per slice for the reconstructed images from the noise-free simulation of the brain phantom, using different axial normalization factors, for the full image (a), the CSF ROI (b), the gray matter ROI (c) and the white matter ROI (d).

ROIs is displayed for the reconstructed images of every simulation. The results are shown in an independent plot for each set of crystal efficiencies. In each plot, the dashed lines represents the best achievable result for both span-1 and span-11 (reconstructed images from the noise-free sinograms and using the N_{C-1} normalization factors). For the crystal set 1 (figure 9(a)), the use of the crystal efficiencies in the normalization had a small impact on the COV since every reconstruction achieved similar values for all the simulated noise levels; except for the one with lowest Poisson noise (mean of 200 counts per bin), where the gap between the COV achieved with N_{C-1} and N_{Tl_mod-1} was larger. For the other simulated crystal sets, the fact of not using the crystal efficiencies in the normalization factors had an increasing impact in the reconstructed images from the simulated sinograms with lower noise. In figure 10, the central slice of the reconstructed images for the simulation with lowest noise are shown, where the impact of not using the crystal efficiencies in the normalization (bottom row) is visible for the sets 2, 3 and 4.

For the simulated brain data, the COV in the putamen, caudate and white matter for every reconstructed image for the different noise levels are shown in figure 11. The simulations with crystal set 1 and 2 showed equivalent results between using the N_{C-1} and the N_{Tl_mod-1} factors. For the images reconstructed with crystals set 3 and 4, not using the crystal efficiencies in the normalization resulted in an increased standard deviation and visible artifacts.

For the case of real data acquired with the Biograph mMR, we computed the mean COV in the background ROIs (μ_{COV}), as well as the COV of the mean values of the ROIs (COV_{μ}). Both parameters are plotted in figure 12 for each slice of the striatal phantom. The reconstructions were evaluated for the N_{C-1} and N_{Tl_mod-1} normalization factors for span-1 sinograms, together

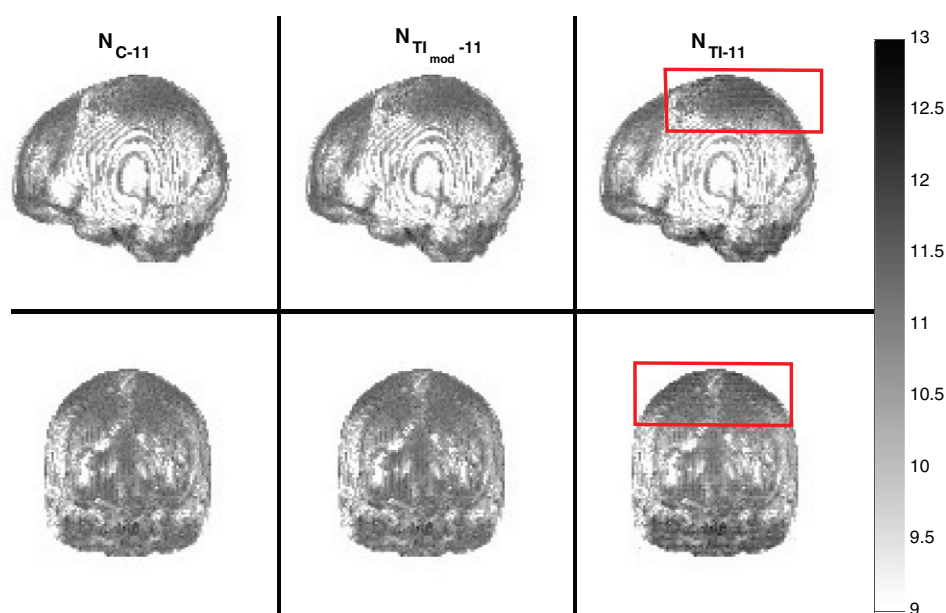


Figure 7. Maximum intensity projections in the sagittal (top) and coronal (bottom) planes for the reconstructed images of the noise-free brain phantom simulations using the true axial factors (N_{C-11}), the proposed axial factors ($N_{TI_{mod}-11}$) and only the span factor as axial component (N_{TI-11}). The regions where artifacts are visible are marked in red.

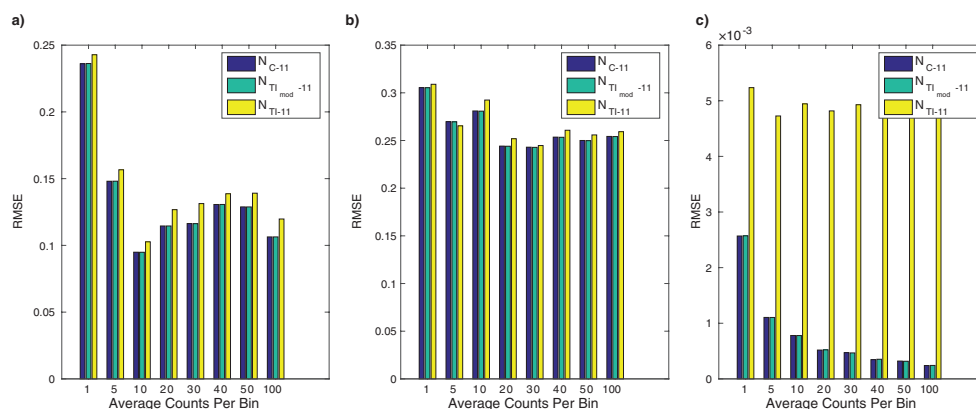


Figure 8. RMSE of the axial mean values for the reconstructed images from the brain phantom simulations with different noise levels and axial factors, for the full image (a), the CSF ROI (b), the gray matter ROI (c) and the white matter ROI (d).

with N_{C-11} , $N_{TI+AX-11}$, $N_{TI_{mod}-11}$ and $N_{C_{random}-11}$ for span-11 sinograms. Moreover, reconstructions without any normalization factor (no-norm) were also included. The parameters used to quantify the noise did not show any notable difference between the different reconstruction methods, except for the reconstructions without any normalization accounted for at all. However, the span-1 reconstructions showed slightly different profiles compared to the span-11 reconstructions. Global μ_{COV} values were computed for each reconstruction and there were not meaningful differences between the normalization methods used.

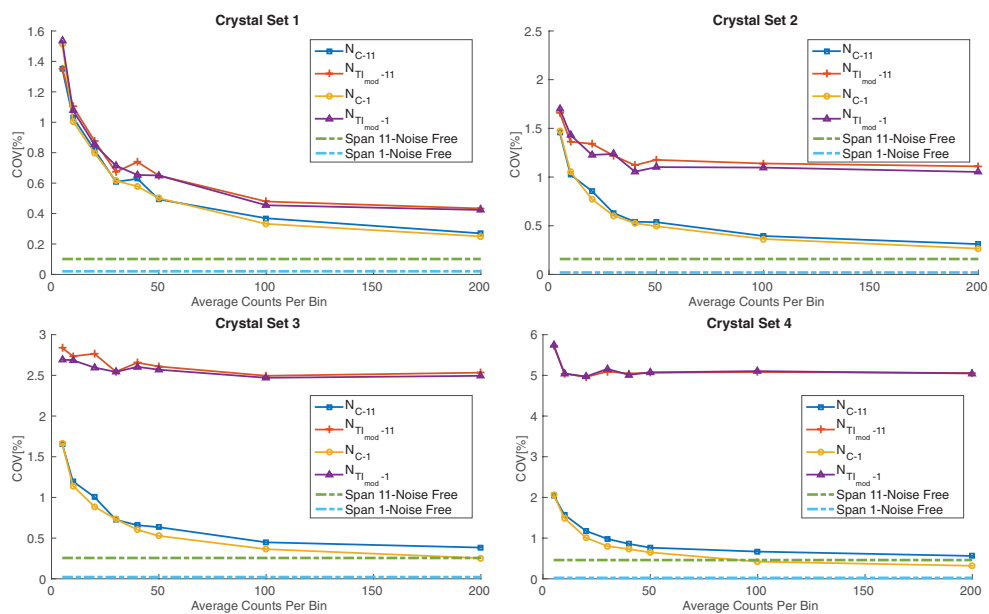


Figure 9. Mean COV of all the ROIs used, for the reconstructed images from the uniform cylinder simulations for the sets 1 (a), 2 (b), 3 (c) and 4 (d) of crystal efficiencies. Each plot show these values for the images reconstructed using the complete normalization factors (N_{C-1} and N_{C-11}) and time-invariant with axial factors ($N_{T_{mod-1}}$ and $N_{T_{mod-11}}$). The dashed lines represents the mean COV of the ROIs achieved in the reconstructed images of the noise-free sinograms and using the N_{C-1} normalization factors.

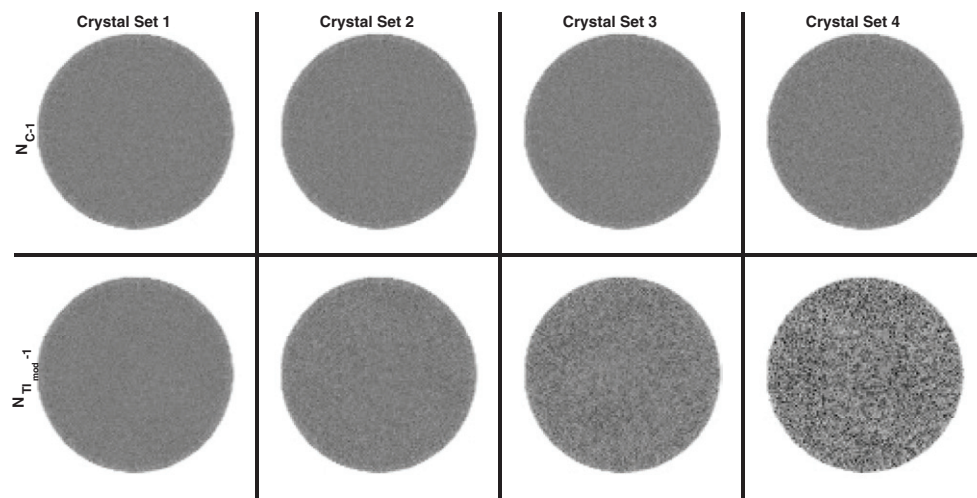


Figure 10. Reconstructed images of the simulated uniform phantom with the lowest noise (200 counts/bin in the sinograms) using N_{C-1} (top) and $N_{T_{mod-1}}$ (bottom) normalization factors. In the columns, from left to right, the images are ordered by the crystal set used in the simulation (1–4).

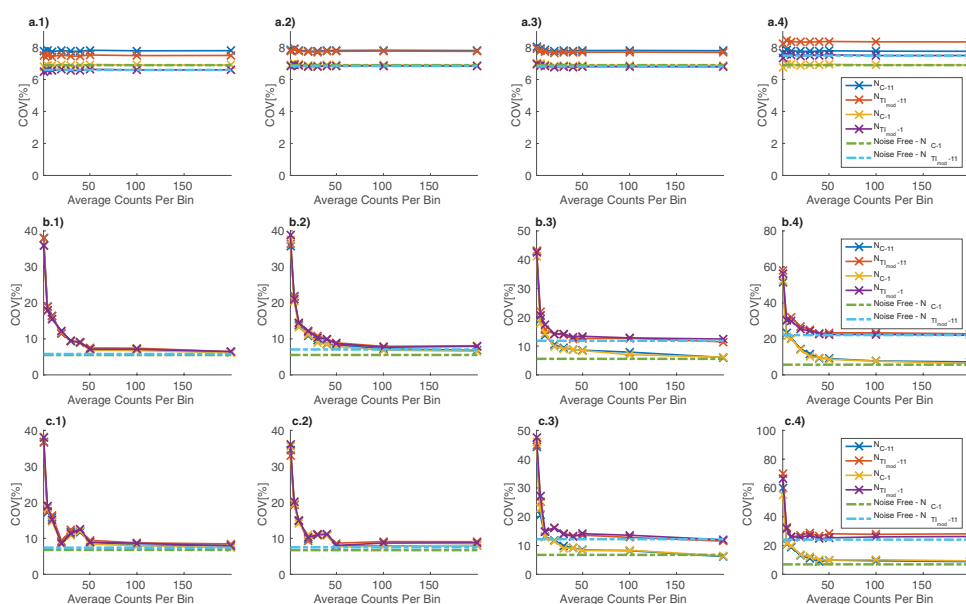


Figure 11. COV in the ROIs of the white matter (top row), the putamen (middle row) and the caudate (bottom row) for the simulated data of the brain phantom. The columns, from left to right, correspond to crystal sets 1–4 used in the simulation. (a.1) White matter—crystal set 1. (a.2) White matter—crystal set 2. (a.3) White matter—crystal set 3. (a.4) White matter—crystal set 4. (b.1) Putamen—crystal set 1. (b.2) Putamen—crystal set 2. (b.3) Putamen—crystal set 3. (b.4) Putamen—crystal set 4. (c.1) Caudate—crystal set 1. (c.2) Caudate—crystal set 2. (c.3) Caudate—crystal set 3. (c.4) Caudate—crystal set 4.

The reconstructed images of the striatal phantom for the main normalization factors evaluated are shown in figure 13. There were no visible differences between all the normalized images, even for an acquisition with very low noise as this one. Ratio images between each reconstructed image and the reconstructed with the standard method in the scanner (N_{C-11}) is shown in figure 14. The reconstructed images of the NEMA phantom are available in figure 15, where the noise of the acquisition had greater influence than the normalization artifacts. Nevertheless, similar quantification results as the striatal phantom were found.

6. Discussion and conclusions

We analysed the variation of the time-variant normalization factors in the Biograph mMR scanner over a period of 230 d and it was observed that both the axial factors and the crystal efficiencies were stable during this period, except for a few cases as were observed in figure 1. Such exceptions could have been produced by a normalization scan done before the scanner had stabilized its temperature. In addition, it was shown that the dispersion of the crystal efficiencies is very low, with a typical coefficient of variation of 3%. Therefore, the crystal interference factors are much more important than the intrinsic crystal efficiencies.

For the axial factors, we presented a method to obtain fixed axial factors that are a good approximation to those available in the normalization files. These axial factors were validated using noise-free simulated data. In a real situation, where noise is present in the images and the axial factors from the normalization file could have changed between acquisitions, the

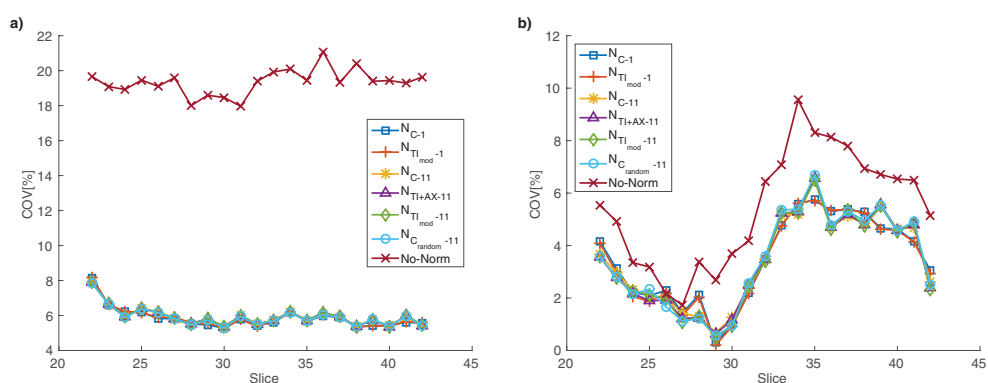


Figure 12. Statistics of the ROIs for each reconstructed image of the scanned striatal phantom: (a) mean COV of the ROIs, per slice. (b) COV of the mean values of the ROIs, per slice.

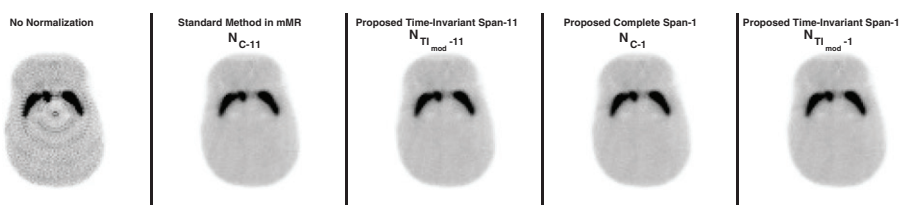


Figure 13. Reconstructed images of the scanned striatal phantom. From left to right, the images reconstructed without normalization (no normalization), with the standard normalization of the scanner (N_{C-11}), the proposed time-invariant factors for span-11 ($N_{TI_{mod}-11}$), the proposed complete factors for span-1 (N_{C-1}) and for the time-invariant for span-1 ($N_{TI_{mod}-1}$).

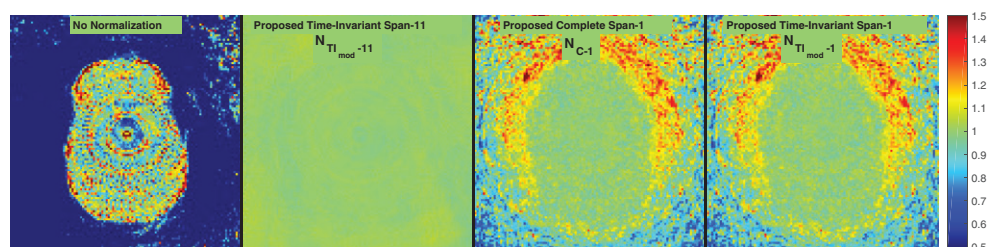


Figure 14. Ratio images between the reconstructed images of the scanned striatal phantom with the different normalization factors and the reconstructed with the standard Biograph mMR normalization. From left to right, the ratio for the images reconstructed without normalization (no normalization), with $N_{TI_{mod}-11}$, with N_{C-1} and with $N_{TI_{mod}-1}$.

difference in image quality when using fixed axial factors compared to those available via the scanner’s CBN could be even lower.

Using simulated data and a similar distribution of crystal efficiencies to the ones observed in the normalization files, we found that the crystal efficiencies can be neglected in the normalization factors, even in images with low noise. A set of crystal efficiencies with a greater range of values would have impact in the reconstructed images, as was shown for sets 2, 3 and

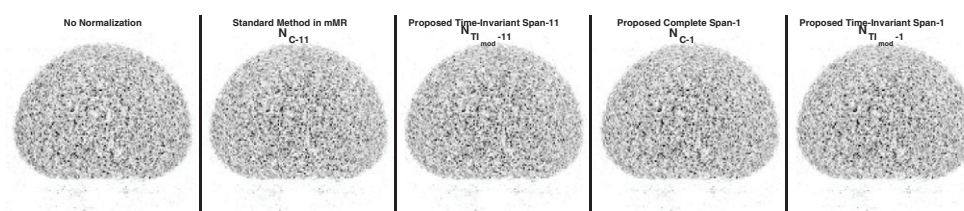


Figure 15. From left to right, the images reconstructed of the scanned NEMA phantom without normalization, with the standard normalization of the scanner (N_{C-11}) and with the proposed factors $N_{T_{mod}-11}$, N_{C-1} and $N_{T_{mod}-11}$.

4. However, for set 2, a set of crystal efficiencies with 5 times the standard deviation found in the Biograph mMR scanner (COV of 15%), this impact was noticeable only in low-noise images. In the experimental data, the span-11 reconstructions achieved slightly lower standard deviation than the span-1 reconstruction. However, this is not necessarily related to the normalization factors since this effect was not observed with simulated data. One possible reason for this outcome is that the use of axial compression reduces the sinogram noise, which results in images with lower noise.

In this study we analysed the normalization of a scanner based on APD detectors. However, the current tendency is to use silicon photomultipliers (SiPMs) as photodetectors instead of APDs. SiPMs also suffer from gain variations with temperature (Roncali and Cherry 2011) and, as a result, a variation in their efficiency. Therefore, a similar time-invariant normalization as the one proposed here could be used in these newer scanners provided the working temperature is stable. In addition, PET detectors that include a temperature-dependent gain control module have already been designed (Xu *et al* 2011) which should facilitate the implementation of a time-invariant normalization method such as the one proposed here.

For scanners with a higher standard deviation in the gain of their photodetectors, an additional method might be necessary to supplement the time-invariant normalization. For example, the Siemens HRRT scanner has crystal efficiencies with a standard deviation of 12%–20% (Rodriguez *et al* 2007), which would correspond to the simulations presented here with crystal sets 2 and 3. An additional strategy needs to be implemented in such situations, such as a self-normalization algorithm (Sibomana *et al* 2009, Salomon *et al* 2012) that could benefit from a time-invariant normalization as the initial estimate of the normalization factors (Belzunce and Reader 2015).

By using real data and the modelled axial factors, we showed that using the proposed time-invariant normalization, that includes the fixed axial factors, in the image reconstruction of the Biograph mMR can achieve equivalent results to using the complete normalization factors. Even in scans with very low noise (e.g. the brain phantom acquisition used in this work), not including the crystal efficiencies in the normalization did not show any notable differences.

To conclude, we can say that successful reconstructions can be achieved with the Biograph mMR without the need to have a daily or weekly normalization scan under normal working conditions. This time-invariant normalization could be implemented in scanners with SiPM as long as they work with a stable temperature or they provide a temperature-dependent gain control. If, however, the crystal efficiencies have a distribution with a COV of 10% or more, the impact would start to be noticeable in low-noise acquisitions and a supplementary method would need to be included.

Acknowledgments

This work was supported by the Engineering and Physical Sciences Research Council [grant number EP/M020142/1]; and the Centre of Excellence in Medical Engineering funded by the Wellcome Trust and EPSRC [grant number WT 088641/Z/09/Z].

References

- Badawi R D, Lodge M A and Marsden P K 1998 Algorithms for calculating detector efficiency normalization coefficients for true coincidences in 3D PET *Phys. Med. Biol.* **43** 189–205
- Badawi R D and Marsden P K 1999 Developments in component-based normalization for 3D PET *Phys. Med. Biol.* **44** 571–94
- Bai B, Li Q, Holdsworth C H, Asma E, Tai Y C, Chatziioannou A and Leahy R M 2002 Model-based normalization for iterative 3D PET image reconstruction *Phys. Med. Biol.* **47** 2773
- Belzunce M A, Verrastro C A, Venialgo E and Cohen I M 2012 Cuda parallel implementation of image reconstruction algorithm for positron emission tomography *Open Med. Imaging J.* **6** 108–18
- Belzunce M A and Reader A J 2015 Self-normalization of 3D PET data by estimating scan-dependent effective crystal efficiencies *IEEE Nuclear Science Symp. Conf. Record*
- Casey M E, Gadagkar H and Newport D 1995 A component based method for normalization in volume PET *Proc. 3rd Int. Meeting of Fully 3D Image Reconstruction in Radiology and Nuclear Medicine* pp 67–71
- Cocosco C A *et al* 1997 BrainWeb: online interface to a 3D MRI simulated brain database *Proc. 3rd Int. Conf. on Functional Mapping of the Human Brain (Copenhagen)* vol 5 p 425
- Delso G, Furst S, Jakoby B, Ladebeck R, Ganter C, Nekolla S G, Schwaiger M and Ziegler S I 2011 Performance measurements of the Siemens mMR integrated whole-body PET/MR scanner *J. Nucl. Med.* **52** 1914–22
- Keereman V, Vanhove C, Van Holen R and Vandenberghe S 2012 Temperature dependence of the LabPET small-animal PET scanner *IEEE Nuclear Science Symp. and Medical Imaging Conf.* pp 2896–901
- Polycarpou I, Thielemans K, Manjeshwar R, Aguiar P, Marsden P and Tsoumpas C 2011 Comparative evaluation of scatter correction in 3D PET using different scatter-level approximations *Ann. Nucl. Med.* **25** 643–9
- Reader A J and Zaidi H 2007 Advances in PET image reconstruction *PET Clin.* **2** 173–90
- Rodriguez M, Liow J-S, Thada S, Sibomana M, Chelikani S, Mulnix T, Johnson C A, Michel C, Barker W C and Carson R E 2007 Count-rate dependent component-based normalization for the HRRT *IEEE Trans. Nucl. Sci.* **54** 486–95
- Roncali E and Cherry S R 2011 Application of silicon photomultipliers to positron emission tomography *Ann. Biomed. Eng.* **39** 1358–77
- Salomon A, Goldschmidt B, Botnar R, Kiessling F and Schulz V 2012 A self-normalization reconstruction technique for PET scans using the positron emission data *IEEE Trans. Med. Imaging* **31** 2234–40
- Sibomana M, Keller S H, Holm S, Bloomfield P M, Blinder S, Hansen S B and Michel C 2009 Component-based normalization for the HRRT for sinogram-mode reconstruction *IEEE Nuclear Science Symp. Conf. Record* pp 2694–7
- Thielemans K, Morel C, Jacobson M W, Kaempf J H and Mustafovic S 2008 Normalisation of histogrammed list mode data *IEEE Trans. Nucl. Sci.* **55** 543–51
- Thielemans K, Tsoumpas C, Mustafovic S, Beisel T, Aguiar P, Dikaios N and Jacobson M W 2012 STIR: software for tomographic image reconstruction release 2 *Phys. Med. Biol.* **57** 867
- Xu T, Fan P, Ma T, Wang S, Deng Z, Lu L and Liu Y 2011 Design and initial performance evaluation of a novel PET detector module based on compact SiPM arrays *IEEE Nuclear Science Symp. and Medical Imaging Conf.* pp 3038–41